Jumping velocity of an electrowetting-actuated droplet: A theoretical and numerical study

Jiayu Du ◉,[1] Nikolaos T. Chamakos ◉,[2] Athanasios G. Papathanasiou ◉,[2]
Yanzhi Li ◉,[1] and Qi Min ◉[1,*]

[1]*Key Laboratory of Advanced Reactor Engineering and Safety of Ministry of Education, Collaborative Innovation Center of Advanced Nuclear Energy Technology, Institute of Nuclear and New Energy Technology, Tsinghua University, Beijing 100084, China*
[2]*School of Chemical Engineering, National Technical University of Athens, 15780 Athens, Greece*

Electrowetting-induced detachment of liquid droplets has application prospects in self-cleaning and digital microfluidics. Although several models have been provided to estimate the critical condition for jumping droplet, there is still a lack of a comprehensive understanding of the energy conversion during detachment process and an accurate prediction of the jumping velocity. In this study, an analytical model adopting the energy balance approach is derived to predict the jumping velocity of an electrowetting-actuated droplet. Our main contribution is to reformulate the models of four energy components including the surface energy, kinetic energy, gravitational potential energy at detachment, as well as the viscous dissipation of entire recoiling. The necessity to correct these energy components has also been physically explained. On the one hand, the droplet morphology at detachment is not spherical but a balloonlike shape, leading to the underestimated surface energy and gravitational potential energy. On the other hand, the previous model that assumes a constant velocity gradient in the bulk results in the overestimated viscous dissipation. Moreover, the kinetic energy of jumping droplet cannot be simply characterized by a rigid body model because of the non-negligible radial velocity. According to the statistics, the correction of the viscous dissipation term contributes the most to reducing prediction error, approaching ∼90%, while the relative errors introduced from other three energy terms are comparable, approaching ∼20%. By testing the prediction results against both present simulations and the experiments in the literature, it is validated that the present model successfully identifies the influence of liquid properties, droplet size, surface wettability, and applied voltage on jumping velocity. The results indicate that the increase in the droplet size causes a nonmonotonic change in jumping velocity, which first increases due to the weakened viscous dissipation, then decreases due to the prominent influence of gravity.

I. INTRODUCTION

Detachment of droplets from a solid surface plays an important role in many practical applications, including condensation heat transfer [1–4], self-cleaning surfaces [5–7] and digital microfluidics (DMF) [8–10]. To achieve a jumping droplet, additional energy needs to be supplied. This extra energy can be provided by several methods, e.g., coalescence [4], vibration [11], electrostatic forces [12], and electrowetting [13]. In view of several advantages such as short response

*Corresponding author: minq86@mail.tsinghua.edu.cn

I. Initial state

II. Voltage on

III. Voltage off

Dielectric θ_Y Electrode

θ_{YL}

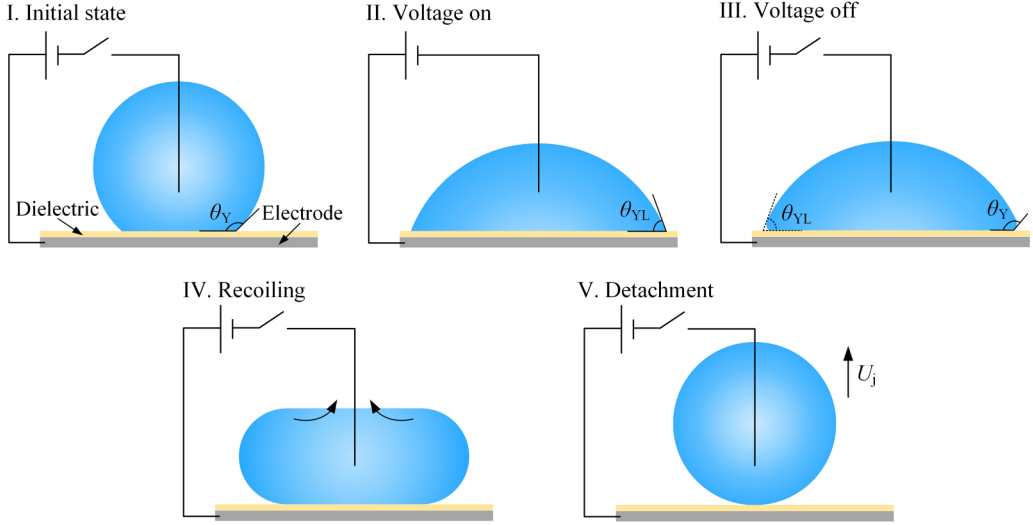θ_{YL} θ_Y

IV. Recoiling

V. Detachment

U_j

FIG. 1. Schematics of the liquid droplet during the electrowetting-induced detachment. (I) A liquid droplet rests on a typical electrowetting device with Young's contact angle, θ_Y. (II) The contact angle reduces to θ_{YL} as a voltage is applied between the droplet and the conductive substrate. (III), (IV) The excess surface energy forces the droplet to recoil as the applied voltage is switched off. (V) The droplet detaches from the solid surface with jumping velocity U_j.

time, low energy consumption, large switching range and high reversibility [14,15], electrowetting has been considered as one of the most efficient methods to induce the detachment.

Lee *et al.* [13] observed droplet jumping on superhydrophobic surface by ac electrowetting and explored how frequencies influenced the jumping height. Since then, extensive studies successively reported the achievement of droplet detachment by single square pulse [16], double square pulse [17], and reversed electrowetting [18]. Figure 1 exhibits the schematic of a typical electrowetting-induced detachment, where a droplet is initially deposited on a conductive substrate coated with a hydrophobic dielectric layer with Young's contact angle θ_Y. When a voltage is applied between the droplet and the electrode below it, the droplet spreads on the dielectric material. This process is driven by the electrowetting force in the vicinity of contact line. The relationship between the new equilibrium contact angle θ_{YL} and the applied voltage V_{app} can be described by the Young-Lippmann equation [19–21], $\cos\theta_{YL} = \cos\theta_Y + \varepsilon_0\,\varepsilon_d V_{app}^2/2d_d\gamma$. Here, $\eta = \varepsilon_0\varepsilon_d V_{app}^2/2d_d\gamma$ is the electrowetting number, $\varepsilon_0 = 8.854 \times 10^{-12}$ F/m is the vacuum permittivity, ε_d is the relative permittivity of the dielectric layer, d is the thickness of dielectric layer, and γ is the liquid-vapor surface tension. As the applied voltage is switched off, the droplet starts recoiling under the action of the capillary force, in which the excess surface energy is converted into kinetic energy and gravitational potential energy. Meanwhile, a portion of kinetic energy is dissipated due to viscous damping. When the applied voltage increases to a threshold value, the droplet can jump off the solid surface.

After the applied voltage is switched off, the effect of electric field vanishes, therefore the dynamic process of droplet retraction becomes a purely hydrodynamic issue. From the perspective of hydrodynamics, the retraction dynamics depends on the balance of inertial, gravity, capillary, and viscous forces. Unraveling how these forces play a role in the dynamic retraction helps to provide a better understanding of the physical mechanism of electrowetting-induced detachment. Since the droplet impact on a solid surface is also a hydrodynamic issue dominated by the balance of afore-mentioned forces, which has been widely studied in the past two decades, it is necessary to identify the important developments of impact dynamics before investigating the electrowetting-induced detachment. Based on the energy balance of surface energy, kinetic energy, and viscous dissipation,

numerous models [22–26] have been established to estimate the maximum spreading diameter of a droplet, providing a useful guide to predict the jumping velocity of an electrowetting-actuated droplet. By considering the motion of a rim, Roisman *et al.* [27] proposed a theoretical model to describe the evolution of contact diameter during the spreading and retraction phase. Moreover, previous studies [28–30] that focused on the bouncing phenomenon after droplet impingement contribute to better understand the dissipation mechanism and enhance droplet jumping. Attractively, Ruiter and co-workers [31,32] reported that a liquid droplet bounced multiple times on both wetting and nonwetting flat surfaces due to the presence of a micrometer-thick air layer sustained below the droplet.

Although the existing studies concerning impact dynamics can provide a fundamental understanding of the electrowetting-induced detachment, the inherent difference between these two physical processes makes it not applicable to directly use the theoretical models of impact dynamics to predict the jumping velocity of electrowetting-induced droplets. Specifically, the initial state of an electrowetting-induced droplet is an unstable, quasistatic spherical cap, while the impacting droplet begins to retract in a lamella shape with internal flow, thus resulting in different dynamic characteristics. In the past decade, extensive work has been devoted to improving energy conversion efficiency and enhancing the jumping phenomenon. Cavalli *et al.* [33] numerically and experimentally analyzed how the energy conversion efficiency is affected by the applied voltage and the surface wettability. Based on the phase field method, Weng *et al.* [34] simulated the nonconductive oil droplet detachment induced by reversed electrowetting and investigated the effects of applied voltage, droplet size, and viscosity on the transient variations of surface energy, kinetic energy, and viscous dissipation during the jumping process. Additionally, the droplet jumping over a topographical bump was systematically studied by Merdasi *et al.* [35,36], who indicated that the detachment could be enhanced by bumps compared with flat surface due to the reduced viscous dissipation.

As the underlying mechanism of electrowetting-induced detachment is understood more clearly, more attention has been attracted on predicting the critical condition of a jumping droplet. According to the balance of the electrically stored surface energy and adhesion work, Lee *et al.* [17] developed a theoretical model to predict the threshold electrowetting number. However, as clarified by Wang *et al.* [18], this model is only valid when the effects of gravity and viscosity are negligible, i.e., for inviscid and small droplets. In practical applications, liquid droplets are generally viscid with a radius up to several millimeters. To obtain a more universal model, the following analytical studies have been conducted. Incorporating the contributions of viscous dissipation and the liquid inertia, Wang *et al.* [18] established a semiempirical model to estimate the critical condition of a nonconductive droplet in an aqueous fluid by reversed electrowetting. A correction factor was introduced to obtain a more accurate recoiling time. Vo *et al.* [37] proposed a theoretical model that considers the bulk dissipation, contact line friction, and the energy loss due to contact line pinning, which included experimental parameters, e.g., the defect size and macroscopic cutoff length of substrate. Zhang *et al.* [38] built a model to quantify the dissipated energy based on the assumption that the velocity gradient in the droplet was constant. Furthermore, according to the previous work of Cavalli *et al.* [33], an analytical model that considers the variation of gravitational potential energy was proposed by Burkhart *et al.* [39]. Nevertheless, they neglected the viscous dissipation of entire recoiling, therefore this model is not applicable for droplets with high viscosity.

Although extensive studies attempted to estimate the critical condition of a jumping droplet, further improvements on accurately quantifying various energy components are still needed, since previous models lacked some detailed information as follows. On the one hand, the surface energy and gravitational potential energy at detachment are formulated on the assumption that the jumping droplet remains in spherical shape, whereas we clarified that the droplet leaves the substrate in a balloonlike shape. On the other hand, we found that the velocity profile among liquid droplets deviates from the assumption of Zhang *et al.* [38], which would result in the overestimated viscous dissipation. Moreover, the kinetic energy at detachment is generally characterized by the rigid body model, whereas we demonstrated that the kinetic energy would be underestimated if this
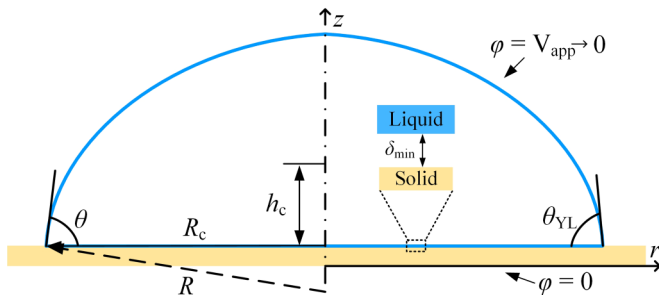
FIG. 2. Schematic of the geometric model of droplet at voltage-off position (left) and the initial state of droplet for present simulation (right).

simplification is adopted, since the kinetic energy provided by the radial velocity is neglected. Additionally, up to now, few studies except Zhang *et al.* [38] proposed a theoretical model to estimate the jumping velocity of electrowetting-induced droplets.

To fill this gap, we theoretically and numerically investigate the electrowetting-induced detachment. The numerical simulation is conducted by an effective, sharp-interface, continuum-level modeling method [40–47] that employs the notion of Derjaguin (or disjoining) pressure. We aim to correct four energy components including the surface energy, kinetic energy, gravitational potential energy at detachment, as well as the viscous dissipation of entire recoiling and develop a prediction model for jumping velocity. Particularly, the formulas of correction coefficients are physically correlated with three dimensionless numbers (Bond number, Ohnesorge number, and electrowetting number) and empirically fitted through regression analysis. The updated model comprehensively accounts for the combined influence of liquid properties, droplet size, surface wettability, and applied voltage, which has been examined by both present simulations and the experiments in the literature.

II. ENERGY BALANCE

It has been aforementioned that the electrowetting-induced detachment is a process where excess surface energy is converted into kinetic energy and gravitational potential energy, accompanying viscous dissipation. In this section, the energy balance approach is presented. According to energy conservation, the surface energy ($E_{s,III}$) and gravitational potential energy ($E_{g,III}$) before the voltage is switched off should be identical to the surface energy ($E_{s,V}$), gravitational potential energy ($E_{g,V}$), and kinetic energy ($E_{k,V}$) at detaching position as well as the viscous dissipation of entire recoiling (W_v) [17,18,38,39]. Namely,

$$E_{k,V} = E_{s,III} + E_{g,III} - E_{s,V} - E_{g,V} - W_v. \qquad (1)$$

Here, we neglect the energy loss due to contact line pinning [37] since the solid surface in the present simulation is ideally smooth and homogeneous. In the following, the expressions of all the energy components will be provided.

To quantify $E_{s,III}$ and $E_{g,III}$, we initially figure out the geometric model of droplet at equilibrium, which can be considered as a spherical cap with volume $V_{drop} = 4\pi R_0^3/3$. According to the geometric model shown in Fig. 2, the radius and contact radius of spherical cap can be evaluated by $R = R_0[4/(2 + \cos\theta)(1 - \cos\theta)^2]^{1/3}$ and $R_c = R\sin\theta$, respectively [37,38,48]. Based on the formulation of net surface energy of a liquid-vapor-solid system, i.e., $E_s = \gamma(A_{LV} - A_{SL}\cos\theta_Y)$, where $A_{LV} = 2\pi R^2(1 - \cos\theta)$ and $A_{SL} = \pi R^2\sin^2\theta$ are the liquid-vapor and liquid-solid contact

area, respectively [38,37,48]. Therefore, the surface energy at the voltage-off and detaching position can be respectively given by

$$E_{s,III} = \pi R_{III}^2 \gamma (2 - 2\cos\theta_{YL} - \sin^2\theta_{YL}\cos\theta_Y),\tag{2}$$

$$E_{s,V} = 4\pi\gamma R_0^2.\tag{3}$$

Here, $R_{III} = kR_0$ is the radius of droplet at voltage-off position and the parameter $k = [4/(2 + \cos\theta_{YL})(1 - \cos\theta_{YL})^2]^{1/3}$ only depends on θ_{YL}.

Furthermore, the height of the center of mass for the spherical cap shown in Fig. 2 can be evaluated by $h_c = (3 + \cos\theta)(1 - \cos\theta)R/4(2 + \cos\theta)$ [39]. Then the gravitational potential energy at the voltage-off and detaching position [39] can be respectively given by

$$E_{g,III} = \tfrac{4}{3}\pi\rho g R_0^3 h_{c,III},\tag{4}$$

$$E_{g,V} = \tfrac{4}{3}\pi\rho g R_0^3 h_{c,V},\tag{5}$$

where ρ is the density of droplet and g is the gravity acceleration. In the above, $h_{c,III} = (3 + \cos\theta_{YL})(1 - \cos\theta_{YL})R_{III}/4(2 + \cos\theta_{YL})$ and $h_{c,V} = R_0$. We note that Eqs. (3) and (5) are only valid when the droplet at the detaching position is spherical. However, in this study we found that the detaching droplet is not spherical but elongated in height, resembling a balloon. The influence of the balloonlike shape on $E_{s,V}$ and $E_{g,V}$ as well as the corrections to these two components will be presented in Sec. IV B.

Previously, Zhang *et al.* [38] quantified the viscous dissipation of entire recoiling by

$$W_v = \int_0^{t_d} \int_{V_{drop}} \Phi dV dt = \int_0^{t_d} \int_{V_{drop}} \frac{\mu}{2}\left(\frac{\partial u_i}{\partial x_j} + \frac{\partial u_j}{\partial x_i}\right)^2 dV dt \approx 12\mu\left(\frac{U_c}{R_0}\right)^2 V_{drop}t_d,\tag{6}$$

where μ is the dynamic viscosity, Φ is the dissipation rate per unit volume, and t_d is the recoiling time, defined as the time interval from the beginning of recoiling to the detaching position. Zhang *et al.* [38] argued that t_d is identical to the inertial-capillary time $\tau_c = (\rho R_0^3/\gamma)^{1/2}$ and the velocity gradient in the droplet bulk is constant, which can be estimated by U_c/R_0 . Here, $U_c = R_0/\tau_c$ is the average recoiling velocity. However, in the present work we found that Eq. (6) deserves further improvement and the details will also be given in Sec. IV B.

The jumping velocity U_j, defined as the vertical velocity of the center of mass at detachment, is commonly used to calculate the kinetic energy:

$$E_{k,V} = \tfrac{1}{2}\rho V_{drop}U_j^2 = \tfrac{2}{3}\pi\rho R_0^3 U_j^2.\tag{7}$$

III. MODELING METHOD

A. Governing equation and boundary conditions

To validate the accuracy and explore the limitation of previous theoretical models, the experimental or numerical results need to be used as a reference. Relying on experimental investigations for computing the energy components would be infeasible and expensive. Thus, a numerical study based on an effective, continuum-level, sharp-interface modeling method is conducted in this work. It should be pointed out that this approach was originally developed in our previous study by Chamakosand co-workers [40–43], which has been extensively applied to investigate the droplet impact dynamics and spontaneous spreading dynamics [44–47]. Since we are committed to predicting the jumping velocity of a liquid droplet, we only simulate the recoiling and detachment when voltage is off. As shown in Fig. 2, a spherical cap droplet is initially rested on dielectric layer with contact angle θ_{YL}. The electric potential of the bottom of the dielectric layer remains zero while the electric potential of the liquid droplet decreases from V_{app} to 0 immediately.

In this study, the liquid droplet is considered as incompressible Newtonian fluid and the fluid flow is governed by Navier-Stokes equation as follows:

$$\rho\left(\frac{\partial \vec{u}}{\partial t} + \vec{u} \cdot \vec{\nabla} \vec{u}\right) = -\vec{\nabla} p + \mu \nabla^2 \vec{u} + \rho \vec{g}, \tag{8a}$$

$$\vec{\nabla} \cdot \vec{u} = 0, \tag{8b}$$

where $\vec{u}$ and p represent the velocity vector and pressure, respectively. According to this modeling method, the liquid-vapor and liquid-solid interfaces are treated in a unified manner, therefore the solution of governing equation depends on the stress boundary condition applied on the unified interface. Specifically, the normal component of total stress is formulated as

$$\tau_{nn} = \vec{n} \cdot \vec{\tau} \cdot \vec{n} = -(p_0 + p_{LS} + p_{el} + 2\kappa\gamma), \tag{9}$$

where $\vec{\tau} = -p\vec{I} + \mu[\vec{\nabla} \vec{u} + (\vec{\nabla} \vec{u})^T]$, $\vec{n}$, κ and p_0 denote the total stress tensor, unit normal vector, local mean curvature, and reference pressure, respectively.

It is worth mentioning that this modeling method incorporates the microscale liquid-solid interaction in the Derjaguin pressure term [49]:

$$p_{LS} = \frac{\gamma w_{LS}}{R_0}\left[\left(\frac{\sigma}{\delta/R_0 + \varepsilon}\right)^{C_1} - \left(\frac{\sigma}{\delta/R_0 + \varepsilon}\right)^{C_2}\right], \tag{10}$$

which resembles the Lennard-Jones potential [50] for molecular dynamics simulations. Due to the presence of Derjaguin pressure, the liquid and solid phases are separated by an intermediate layer with thickness $\delta_{min} = R_0(\sigma - \varepsilon)$ (see Fig. 2). In the above equation, C_1 and C_2 regulate the active range of p_{LS}. The Euclidean distance from the solid surface δ determines whether p_{LS} is attractive (modeling van der Waals interactions, for large δ) or repulsive (modeling steric forces and electrostatic interactions determined by an overlapping of the electrical double layers, for small δ). Particularly, at $\delta = \delta_{min}$, the repulsive and attractive forces balance each other, i.e., $p_{LS} = 0$. For a perfectly smooth substrate, δ can be simply characterized by the vertical distance from solid surface, while for a structured substrate, δ can be obtained from the solution of the eikonal equation [51].

Besides, the depth of the potential well is proportional to the wetting parameter w_{LS}, which has a one-to-one correlation with Young's contact angle. The formulation of w_{LS} is expressed as

$$w_{LS} = \frac{(C_1 - 1)(C_2 - 1)(1 + \cos\theta_Y)}{\sigma(C_1 - C_2)}. \tag{11}$$

The significance of wetting parameter is to avoid the specification of explicit contact angle boundary condition to unknown, multiple contact lines on structured surface. Under the combined actions of Derjaguin and capillary pressure, the dynamic contact angle can emerge in a more physical manner.

The effect of electric field is incorporated in the form of electrostatic pressure p_{el}, providing a negative component for the normal component of total stress. The electrostatic pressure is given by $p_{el} = \varepsilon_0 e^2/2$, where e is the magnitude of the electric field strength $\vec{e} = -\vec{\nabla}\varphi$. Here, φ is the electric potential, computed by solving the Gauss's law for electricity,

$$\vec{\nabla} \cdot (\varepsilon_0 \varepsilon_r \vec{\nabla}\varphi) = 0. \tag{12}$$

Since the droplet is regarded as an ideal conductor, the electric potential is solved only in the ambient phase (air for this study) and dielectric material. For simplicity, a continuous function is used to describe the relative permittivity, i.e.,

$$\varepsilon_r = (\varepsilon_a - \varepsilon_d)\tanh\left(5\frac{\delta}{\delta_{min}}\right) + \varepsilon_d. \tag{13}$$

TABLE I. Liquid physical properties of water and two glycerol-water mixtures.

Glycerol concentration	ρ (kg/m^3)	γ (mN/m)	μ (mPa s)
0 wt %	998	72.8	1.0
20 wt %	1043	71.0	1.8
40 wt %	1099	69.0	3.7

This expression can ensure that ε_r becomes ε_a and ε_d in the ambient phase and dielectric layer, respectively. Moreover, ε_r undergoes a sharp transition in the intermediate layer between droplet and dielectric material. To solve Eq. (12), $\varphi = V_{app}$ is applied at the droplet interface, where V_{app} is the voltage between conductive droplet and electrode. The boundary condition $\varphi = 0$ is applied at the bottom of the dielectric layer. Although the actuated stage of the liquid droplet is not considered in the present work, the electrostatic pressure is solved to validate the reliability of this modeling method (see Sec. III C).

Moreover, the Navier slip boundary condition is used to prevent the droplet freely slipping on the solid surface. Specifically, the tangential stress applied on the unified interface is expressed as

$$\tau_{nt} = \vec{n} \cdot \vec{\tau} \cdot \vec{t} = \xi_{eff}(\vec{t} \cdot \vec{u}). \tag{14}$$

In the above, $\vec{t}$ is the unit tangential vector and ξ_{eff} denotes the effective slip coefficient, which is only active in the vicinity of substrate and formulated as

$$\xi_{eff} = \frac{\mu \xi_{sl}}{R_0} \left\{ 1 - \tanh\left[5\left(\frac{\delta}{\delta_{min}} - 1\right) \right] \right\}, \tag{15}$$

Here, ξ_{sl} denotes the dimensionless slip parameter, corresponding to the slip length, R_0/ξ_{sl}. This continuous formulation enables the transition from a free slip boundary condition imposed on the liquid-gas interface to a partial slip boundary condition imposed on the liquid-solid interface. Finally, the moving mesh method is employed to accurately capture the movement of interface, which follows the kinematic equation below:

$$(\vec{u}_{mesh} - \vec{u}) \cdot \vec{n} = 0. \tag{16}$$

Here, $\vec{u}_{mesh}$ represents the velocity vector of the meshes at the unified interface, which are refined to ensure the accuracy of computing results. Besides, when the mesh quality drops to the threshold, automatic remeshing will be enabled.

B. Initialization and modeling setup

In this study, we investigate the detachment of water and two glycerol-water mixtures. The physical properties of working fluids under room temperature are given in Table I [52]. The characteristic radius of liquid droplet R_0 ranges 10 μm–1.40 mm. Furthermore, the substrate wettability is fixed with $\theta_Y = 130°$ while θ_{YL} ranges $80°$–$90°$, corresponding to electrowetting number $\eta = 0.643$–0.816. The parameters relevant to numerical simulation are consistent with our previous work [40–47], i.e., $C_1 = 12$, $C_2 = 10$, $\sigma = 9 \times 10^{-3}$, $\varepsilon = 8 \times 10^{-3}$, and $\xi_{sl} = 1000$. In addition, the solution of the governing equations and the setting of the boundary conditions are realized in COMSOL Multiphysics® software. The governing equations are discretized using the finite element method (FEM) and integrated in time with the implicit Euler method.

C. Validation

To validate the reliability of this modeling method, we simulate the electrowetting-induced detachment of a 5-μL NaCl droplet from a hydrophobic surface with $\theta_Y = 116°$ at a 135 V ($\eta = 0.73$)
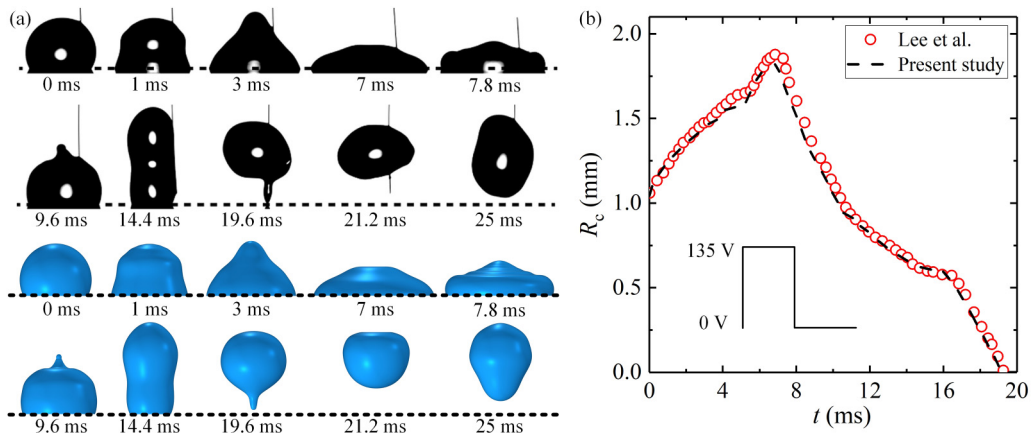
FIG. 3. Comparison of the experiment study by Lee *et al.* [17] with present simulation. (a) Consecutive side-view images of droplet detachment. (b) Temporal evolution of contact radius R_c.

square pulse with a 7-ms pulse width. The comparison of the present simulation with the experimental study of Lee *et al.* [17]. is shown in Figs. 3(a) and 3(b), which exhibits the variation of droplet shape and contact radius, respectively. It is noteworthy that the present simulation agrees well with Lee's study [17] both qualitatively and quantitatively. The slight discrepancy between the experimental and numerical results may arise from the presence of needle electrode in the experiment. Under the actuation of electrostatic pressure, the droplet spreads to the maximum at $\sim$7 ms, accompanying with the generation of capillary wave. Then it retracts dramatically and detaches from the solid surface at $\sim$19.6 ms. According to the validation above, we can confirm that the modeling method used in this study is capable to efficiently simulate the electrowetting-induced detachment of a liquid droplet.

IV. RESULTS AND DISCUSSION

A. Retraction dynamics of electrowetting-actuated droplets

To comprehensively investigate the retraction dynamics of electrowetting-induced detachment, we first exhibit the temporal evolution of contact radius during initial recoiling in Figs. 4(a) and 4(b), which illustrate the effects of liquid properties and applied voltage, respectively. Here, the contact radius R_c is normalized by the contact radius when voltage is switched off $R_{c,III}$, while t is normalized by the inertial-capillary time $\tau_c = (\rho R_0^3/\gamma)^{1/2}$. Notably, the normalized evolutions are basically independent of liquid properties, droplet size, and applied voltage, which means that the initial recoiling is dominated by the balance of inertial pressure $\sim\rho(dR_c/dt)^2$ and capillary pressure $\sim\gamma R_0/R_c^2$. It has been confirmed that the scaling law $R_c/R_0 = C(t/\tau_c)^\alpha$ can describe the initial spreading dynamics in the inertial regime [45,52–54], where the spreading exponent α is only related to substrate wettability. Inspired by these studies, we speculate that a similar scaling law $R_c/R_{c,III} - 1 = C(t/\tau_c)^\alpha$ can determine the initial recoiling of electrowetting-induced detachment. Through regression analysis, we obtain an empirical model $R_c/R_{c,III} = 1 - 0.425(t/\tau_c)^{0.592}$ (solid lines in Fig. 4) that agrees well with the numerical results. The almost constant recoiling exponent can be ascribed to the fixed substrate wettability, which will increase as the solid surface becomes more hydrophobic.

Next, the droplet deformation and energy variation in the recoiling process are systematically analyzed. Figures 5(a) and 5(b) show the snapshots and velocity contour of 20-wt % glycerol droplets with $R_0 = 0.9$ mm and $R_0 = 0.1$ mm, respectively. Correspondingly, the temporal evolution of the energy difference from the voltage-off state $\Delta E = E - E_{III}$ ($E = E_k, E_g, E_s, W_v$) is
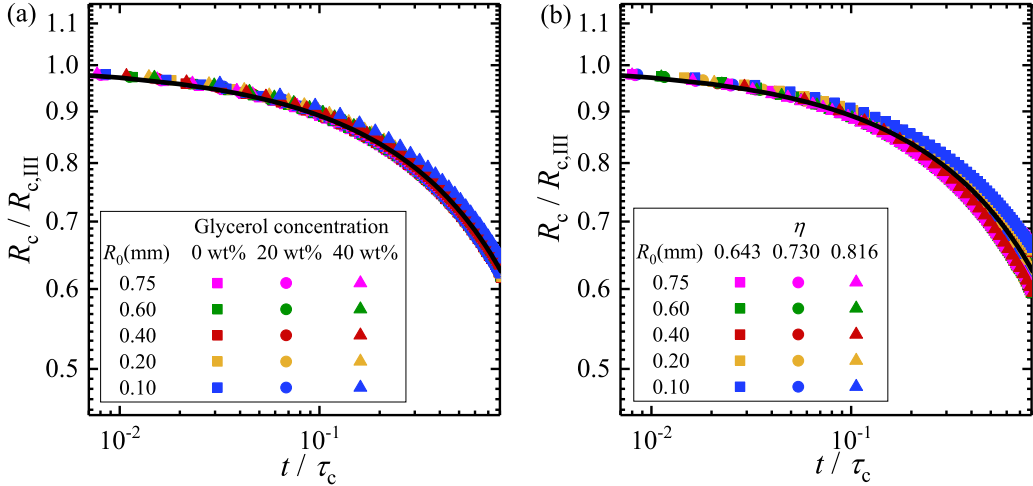
FIG. 4. Temporal evolutions of the normalized contact radius $R_c/R_{c,III}$ with normalized time t/τ_c in log-log scale. (a) Various glycerol-water mixtures under $\theta_{YL} = 85°$. (b) 20 wt % glycerol under various θ_{YL}. The solid lines represent the empirical model, $R_c/R_{c,III} = 1 - 0.425 \, (t/\tau_c)^{0.592}$.

exhibited in Figs. 6(a) and 6(b). Particularly, ΔE is normalized by the initially available excess surface energy $E_{exc} = E_{s,III} - E_{s,I}$ while t is normalized by τ_c. At early recoiling, capillary waves are observed to propagate along the droplet interface (see the snapshots at $t/\tau_c = 0.098$ and 0.263 in Fig. 5). With the decrease of R_0, capillary waves are less visible due to the higher viscous damping. Simultaneously, the fluctuation of E_k and E_s is less significant (see Fig. 6). The capillary wave propagating to the top can induce an upward velocity and the higher pressure at the top can further generate a downward velocity, eventually leading to the emergence of a concave (see the snapshots at $t/\tau_c = 0.495$ in Fig. 5).

As shown in Fig. 6, E_s decreases rapidly before $t/\tau_c \sim 0.795$ and most of it is converted into E_k, while the rest is converted into E_g and W_v. At $t/\tau_c \sim 0.795$, E_k and E_s approach the maximum and minimum value, respectively. The normalized time to reach the extreme value of E_k and E_s is almost independent of R_0. Meanwhile, the droplet shape is quite close to the one at equilibrium
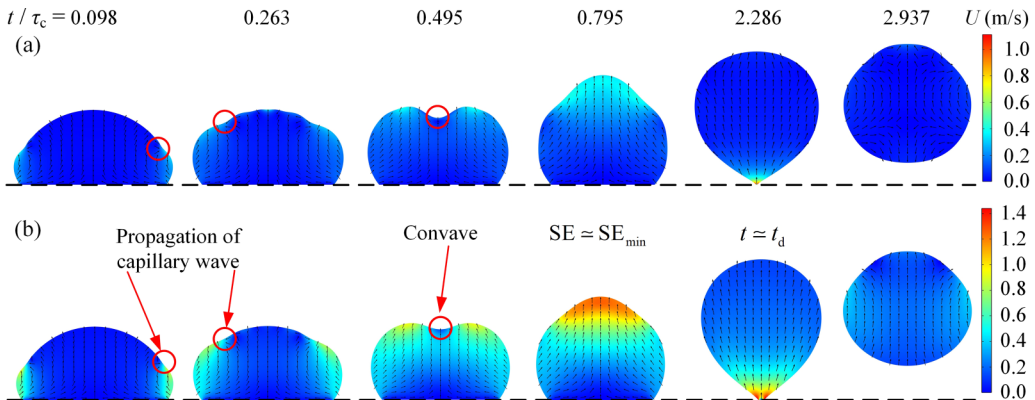

FIG. 5. Sectional views of the velocity field of 20 wt % glycerol droplets with (a) $R_0 = 0.9$ mm and (b) $R_0 = 0.1$ mm under $\theta_{YL} = 85°$. The snapshots are colored by the magnitude of velocity and the arrows only indicate the direction of velocity.
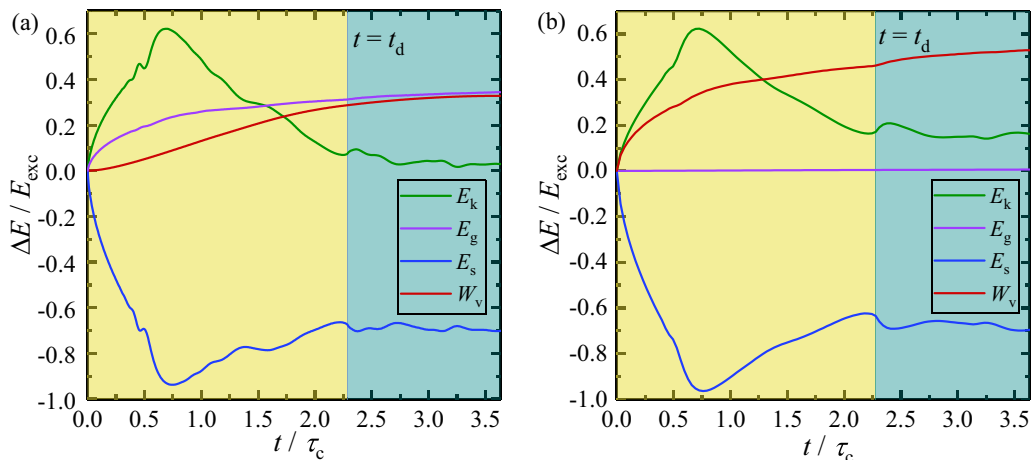
FIG. 6. Energy difference from the voltage-off state ΔE normalized by the excess surface energy E_{exc} versus normalized time t/τ_c for 20 wt % glycerol droplets with (a) $R_0 = 0.9$ mm and (b) $R_0 = 0.1$ mm under $\theta_{YL} = 85°$.

state with Young's contact angle, because $\Delta E_s/E_{exc} \sim -1$. From $t/\tau_c \sim 0.795$ to the moment when the droplet leaves the solid surface, the droplet needs to overcome the adhesion work and gravity, therefore the conversion of E_k into E_s and E_g is observed in Fig. 6. Simultaneously, W_v continues to increase even though the increasing rate gradually slows down. The droplet is about to detach from the solid surface at $t/\tau_c \sim 2.286$ and the dominant factor of recoiling time will be explained in the following section. It is noteworthy that during the recoiling process, the kinetic energy dissipated by viscosity is comparable to the surface energy converted into kinetic energy and the variation of gravitational potential energy, which is prominent for large droplet. Hence, we further confirm the necessity of taking the influence of gravity and viscosity into account in the energy balance model. Additionally, in contrast with Fig. 6(a), the variation of gravitational potential energy in Fig. 6(b) is quite small. In terms of the Bond number Bo $= \rho g D_0^2/\gamma$ (the ratio of gravity to surface tension), as R_0 decreases from 0.9 to 0.1 mm, correspondingly, Bo is reduced by about two orders of magnitude (from 0.47 to 0.006), which means that the effect of gravity becomes very weak.

As shown from the snapshots at $t/\tau_c = 2.286$ in Fig. 5, the droplet shape at detachment is not a standard sphere but a balloonlike shape. Although the balloonlike shape has been observed in previous experiments [10,17,18,37,39,55] and simulations [33,34,56,57], its influence on the energy balance model has not been clarified until now. We analyze that the balloonlike shape gives rise to the increase of liquid-vapor interface A_{LV} and the height of the center of mass h_c, which can induce the underestimation of $E_{s,V}$ and $E_{g,V}$, i.e., Eqs. (3) and (5). According to the velocity contour in Fig. 5, it is also worth mentioning that the velocity gradient during recoiling is nonuniform and the kinetic energy at the detaching position is not completely supplied by vertical velocity, which means that the formulation of W_v and $E_{k,V}$, i.e., Eqs. (6) and (7), is also not sufficiently accurate. Therefore, exploring how to correct these theoretical models is the priority, which will be presented in the following section.

After leaving the solid surface, most kinetic energy would transform into gravitational potential energy, while the rest would be dissipated by viscosity (see continuously increasing W_v in Fig. 6), since the droplet oscillates repeatedly due to the unbalanced pressure in the bulk. The droplet would bounce on the solid surface many times until all the kinetic energy is dissipated viscously. However, the energy variation after detachment is not the focus of this study, which will be systematically analyzed in our future work.
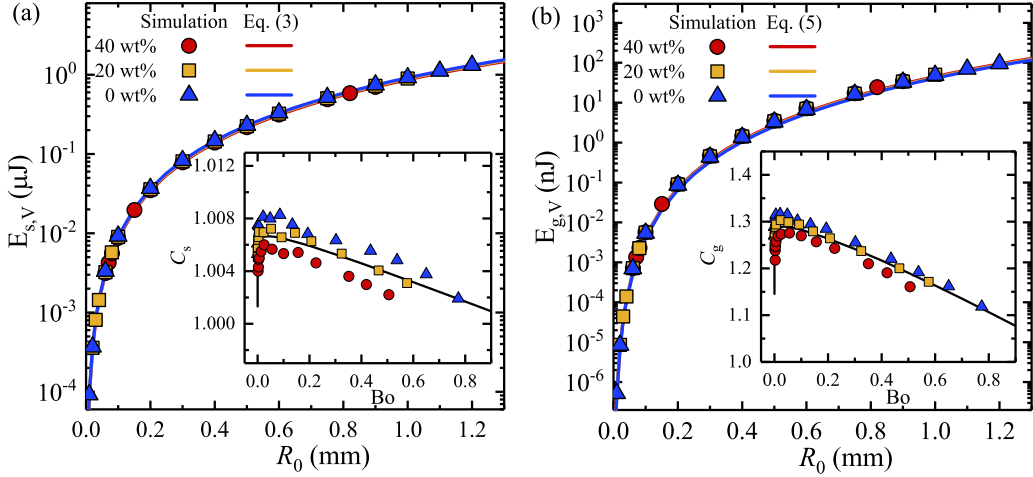
FIG. 7. Comparison of the (a) theoretical surface energy at detachment $E_{s,V}$ and (b) gravitational energy at detachment $E_{g,V}$ respectively estimated by Eqs. (3) and (5) (solid line) with the ones measured in the present simulation (solid symbol) under $\theta_{YL} = 85°$. The insets show the correction coefficients C_s and C_g as a function of Bond number Bo, where the solid line denotes an empirical model fitted by $a\text{Bo}^b + c\text{Bo}^d$.

B. Energy component corrections

In the above, we have demonstrated that the assumption or simplification in the literature deviates from practical conditions. Therefore, modifying conventional models becomes an urgent issue to deal with. In this section, four empirical models have been established, associating correction coefficients with three dimensionless numbers, i.e., Bond number $\text{Bo} = \rho g D_0^2 / \gamma$ (the ratio of gravity to surface tension), Ohnesorge number $\text{Oh} = \mu / (\rho R_0 \gamma)^{1/2}$ (the ratio of viscous force to inertial force and surface tension), and electrowetting number $\eta = \varepsilon_0 \varepsilon_d V_{app}^2 / 2 d_d \gamma$ (a dimensionless number that characterizes the influence of applied voltage), and normalized jumping velocity U_j/U_c. Here, $D_0 = 2R_0$ is the initial diameter of droplet. To ensure that each correction factor is not only numerically accurate but also physically meaningful, we use specific parameters instead of all parameters for fitting and explain the reason from a physical point of view.

It is known that $E_{s,V}$ and $E_{g,V}$ are determined by the droplet morphology at detachment. Since it is tough work to parametrize the droplet profile by a universal, analytical model, we introduce correction coefficients C_s and C_g to modify $E_{s,V}$ and $E_{g,V}$, respectively. The values of correction coefficients are calculated by dividing $E_{s,V}$ and $E_{g,V}$ measured in the present simulation by the ones estimated by Eqs. (3) and (5). During the retraction process, the three-phase contact line cannot detach from the solid surface due to adherence (related to surface tension), while the liquid-vapor interface moves upwards freely, which promotes the elongation of the droplet. On the contrary, gravity inhibits the elongation. Since Bo describes the balance of gravity and surface tension, the correction coefficients C_s and C_g as a function of Bo are illustrated in the insets of Figs. 7(a) and 7(b), respectively, where the comparison of simulated $E_{s,V}$ and $E_{g,V}$ with the theoretical ones estimated by Eqs. (3) and (5) is also shown. It is seen that the viscosity of liquid droplet hardly affects $E_{s,V}$ and $E_{g,V}$. More importantly, both C_s and C_g of different liquids are collapsed into a single curve by Bo. As $C_s, C_g > 1$, the theoretical results of Eqs. (3) and (5) are both underestimated, thus proving our aforementioned speculations. Even though the relative deviation of Eq. (3) ($\sim 0.5\%$) is extremely small and negligible compared with the one of Eq. (5) ($\sim 25\%$), $E_{s,V}$ is much larger than $E_{g,V}$, especially for a small droplet (up to five orders of magnitude). Consequently, the underestimation of $E_{s,V}$ cannot be completely ignored.
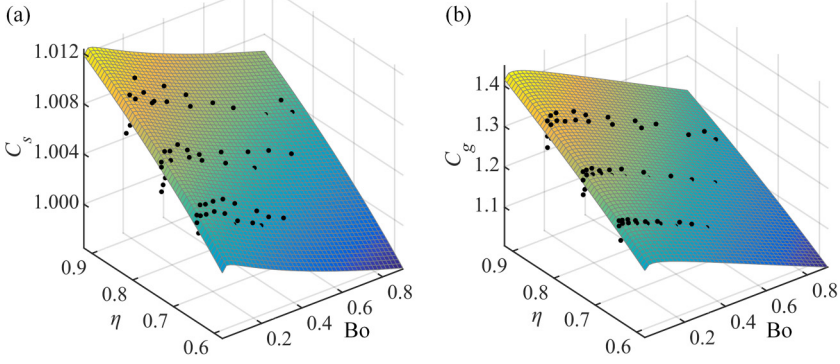
FIG. 8. Comparison of the empirical models of (a) C_s and (b) C_g, i.e., Eqs. (17) and (18), with the numerical results (solid symbol).

The nonmonotonic variation of C_s and C_g with Bo indicates that as the effect of gravity becomes more dominant, the aspect ratio of a liquid droplet first increases, then decreases. Through regression analysis, C_s and C_g can be fitted by an empirical correlation, $a\mathrm{Bo}^b + c\mathrm{Bo}^d$ [see the solid line in the insets of Figs. 7(a) and 7(b)]. Because the droplet morphology at detachment is also closely related to the initial condition of the droplet, which is determined by the applied voltage [18,39], C_s and C_g should also be a function of the electrowetting number, which is found to follow $\sim\eta^f$. Based on the statistical analysis above, C_s and C_g can finally be described as $(a\mathrm{Bo}^b + c\mathrm{Bo}^d)\eta^f$ and the final forms of the empirical model are fitted by

$$C_s = (-0.011\mathrm{Bo}^{0.522} + 1.019\mathrm{Bo}^{0.00086})\eta^{0.0218}, \tag{17}$$

$$C_g = (-0.308\mathrm{Bo}^{0.913} + 1.539\mathrm{Bo}^{0.0090})\eta^{0.413}. \tag{18}$$

Figures 8(a) and 8(b) compare the empirical models above with the numerical results. It is noteworthy that both Eqs. (17) and (18) are in good agreement with the present simulations, proving the reliability of these two models.

As aforementioned in the Sec. II, Zhang *et al.* [38] pointed out that the recoiling time t_d was identical to τ_c. To validate their elaboration, Fig. 9(a) shows the variation of t_d with τ_c. It is seen that t_d is not identical to τ_c but actually linear with it. More importantly, this conclusion is always valid for the cases with different liquid properties, droplet size, and applied voltage. Through regression analysis based on the least squares method, an empirical correlation $t_d = (2.37 \pm 0.20)\,\tau_c$ is obtained.

According to Eq. (6), the formulation of the viscous dissipation before detachment can be given by

$$W_v = 12\mu\left(\frac{U_c}{R_0}\right)^2 V_{\mathrm{drop}}t_d \approx 36.8\pi\mu\sqrt{\frac{\gamma R_0^3}{\rho}}. \tag{19}$$

To verify its efficiency, we compare Eq. (19) with the dissipated energy measured in the present simulation,

$$W_v = \int_0^{t_d} \int_{V_{\mathrm{drop}}} \Phi\, dV\, dt, \tag{20}$$

where

$$\Phi = 2\mu\left\{\left(\frac{\partial u_r}{\partial r}\right)^2 + \left(\frac{\partial u_z}{\partial z}\right)^2 + \left(\frac{u_r}{r}\right)^2 + \frac{1}{2}\left[\left(\frac{\partial u_z}{\partial r}\right)^2 + \left(\frac{\partial u_r}{\partial z}\right)^2 + 2\frac{\partial u_z}{\partial r}\frac{\partial u_r}{\partial z}\right]\right\}. \tag{21}$$
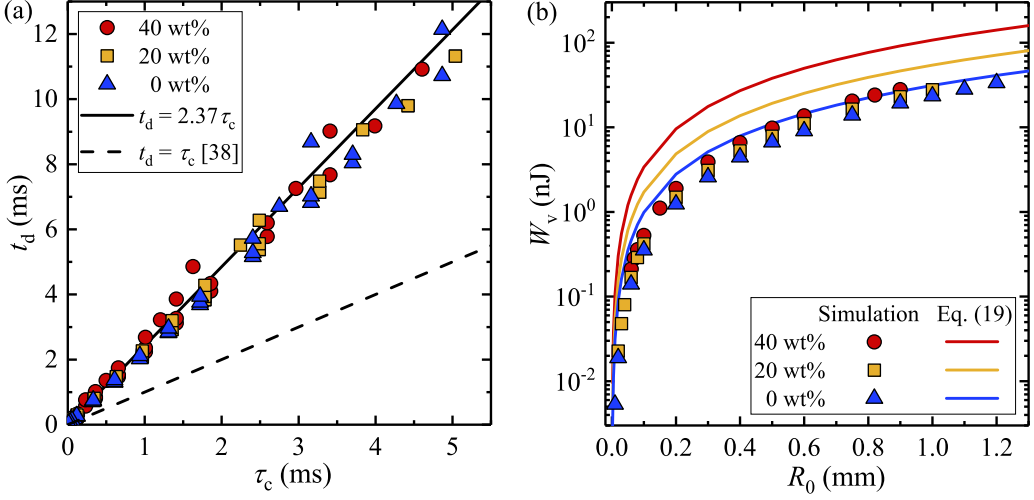
FIG. 9. (a) Recoiling time t_d as a function of inertial-capillary time τ_c. The dashed and solid lines denote the previous and present models of t_d, respectively. (b) Comparison of viscous dissipation estimated by Eq. (19) (solid line) with the simulated ones (solid symbol) under $\theta_{YL} = 85°$.

As shown in Fig. 9(b), W_v is generally overestimated by Eq. (19) and the deviation becomes more prominent with the increase of viscosity. The assumption of constant velocity gradient may account for this overestimation.

To modify Eq. (19), we introduce a correction coefficient C_v. As analyzed above, the computing error of Eq. (19) arises from the quantification of velocity gradient. From the perspective of hydrodynamics, the velocity profile of droplet depends on the balance of inertial pressure $\sim \rho(dR_c/dt)^2$, capillary pressure $\sim \gamma R_0/R_c^2$, and viscous stress $\sim \mu(dR_c/dt)/l$, where l is a characteristic length scale that determines the effective range of viscous stress [53,58]. Additionally, previous studies [33,34,36] have numerically indicated that the velocity field is also closely related to applied voltage (or the initial condition of droplet). Since the Ohnesorge number $Oh = \mu/(\rho R_0 \gamma)^{1/2}$ unifies the relative strength of viscous force with inertial force and capillary force, and electrowetting number $\eta = \varepsilon_0 \varepsilon_d V_{app}^2/2d_d\gamma$ characterizes the influence of applied voltage, we speculate that C_v is governed by Oh and η.

The log-log plot of C_v versus Oh under various η is exhibited in Fig. 10(a). It is observed that C_v is generally below unit. The modification of W_v is not needed only when Oh is sufficiently small, corresponding to low viscosity, high surface tension, and large droplet size. Besides, C_v shows positive and negative correlation with η and Oh, respectively, which may be attributed to the enhanced shear stress. Attractively, for various liquids and applied voltage, C_v scales as $\sim Oh^{-0.656}$. Similar to C_s and C_g, C_v is also found to follow a power law of η. Through regression analysis, C_v are finally fitted by

$$C_v = 0.0388 Oh^{-0.656} \eta^{2.212}. \tag{22}$$

Then the modified viscous dissipation can be given by

$$W_v = 36.8 C_v \pi \mu \sqrt{\frac{\gamma R_0^3}{\rho}}. \tag{23}$$

Figure 10(b) compares the estimation of Eq. (23) with the simulated W_v. Notably, Eq. (23) agrees well with the numerical result and the accuracy of present model is significantly improved, thus confirming the reliability of Eq. (22).
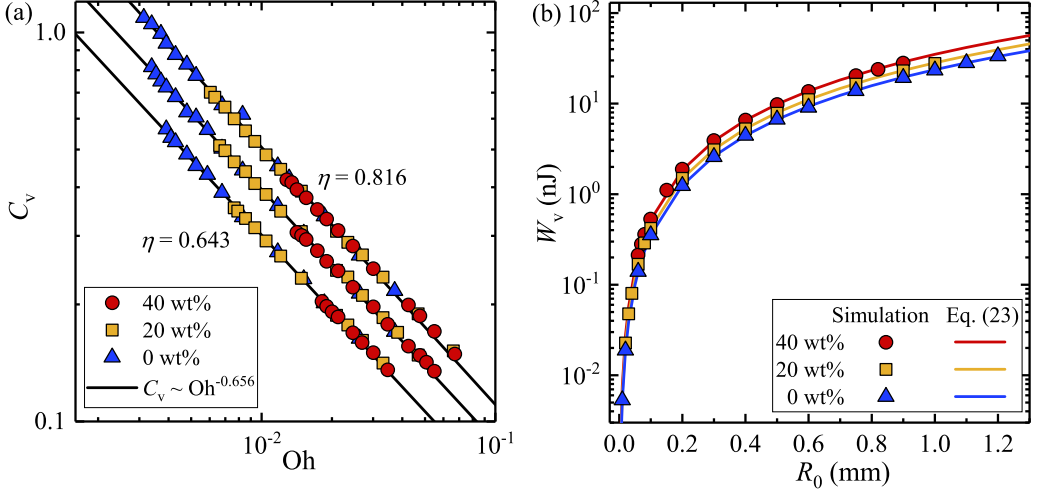
FIG. 10. (a) Correction coefficient C_v as a function of Ohnesorge number Oh under various η. The solid lines represent the power law, $\sim Oh^{-0.656}$. (b) Comparison of the viscous dissipation estimated by Eq. (23) (solid line) with the simulated ones (solid symbol) under $\theta_{YL} = 85°$.

In Sec. IV A, we have clarified that $E_{k,V}$ cannot be simply determined by Eq. (7) due to the contribution of radial velocity. The kinetic energy in the present simulation is integrated by

$$E_{k,V} = \int_{V_{drop}} \frac{1}{2} \rho U^2 dV. \tag{24}$$

To examine our demonstration, Fig. 11(a) shows the comparison of Eq. (24) with the theoretical $E_{k,V}$ estimated by Eq. (7). It can be seen that although both the theoretical and simulated $E_{k,V}$ are nonmonotonic with R_0, the theoretical ones are underestimated especially for low-viscosity liquid. Hence, we introduce a correction coefficient C_k to eliminate this underestimation. Then Eq. (7) is
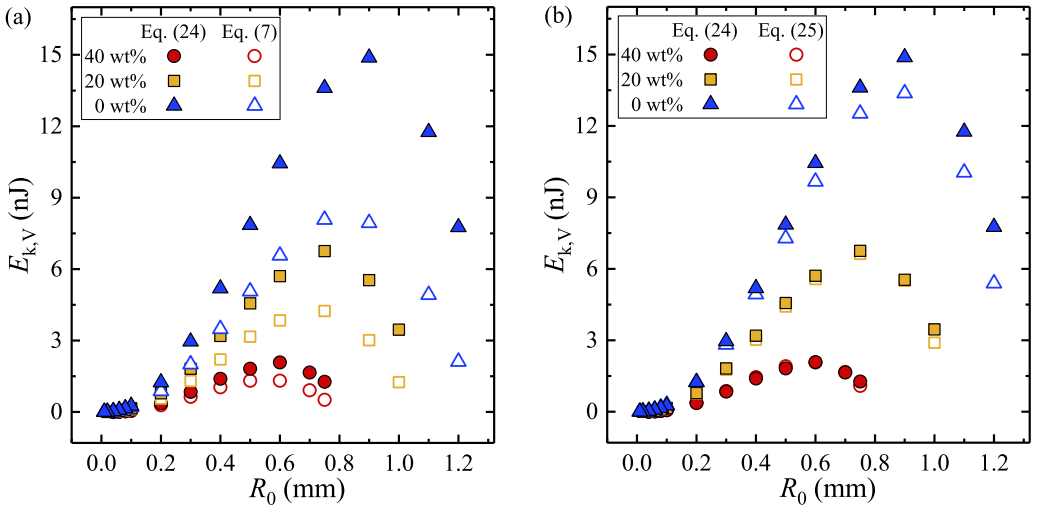

FIG. 11. Comparison of the kinetic energy estimated by (a) Eq. (7) and (b) Eq. (25) (hollow symbol) with the simulated ones measured by Eq. (24) (solid symbol) under $\theta_{YL} = 85°$.

modified as

$$E_{k,V} = \frac{2}{3}\pi C_k \rho R_0^3 U_j^2. \tag{25}$$

Figure 11(a) also illustrates that the deviation between Eqs. (7) and (24) increases with increasing $E_{k,V}$. In other word, C_k may be positively related to $E_{k,V}$. However, since the value of $E_{k,V}$ is determined by multiple parameters (e.g., liquid properties, droplet radius, applied voltage, and surface wettability), using all of these parameters to establish the empirical model of C_k is complicated and impractical. Therefore, in terms of the positive correlation of $E_{k,V}$ with normalized jumping velocity U_j/U_c, we decide to characterize C_k by U_j/U_c. Nevertheless, it is still very difficult to characterize C_k as a single-valued function of U_j/U_c. To minimize the prediction error, we finally think it is more appropriate to express C_k as a function of U_j/U_c and η. Through regression analysis, C_k is fitted by

$$C_k = 1.182\eta^{1.224}\left(\frac{U_j}{U_c}\right)^{-0.437}. \tag{26}$$

As shown in Fig. 11(b), the prediction of Eq. (25) is in good agreement with the numerical results, therefore all energy components have been reformulated so far.

C. Model development

According to the corrections above, by substituting Eq. (2)–(5), (17), (18), (22), (23), (25), and (26) into Eq. (1), the updated energy balance model is developed in the following:

$$\pi R_{III}^2 \gamma (2 - 2\cos\theta_{YL} - \sin^2\theta_{YL}\cos\theta_Y) + \frac{4}{3}\pi \rho g R_0^3 \frac{(3 + \cos\theta_{YL})(1 - \cos\theta_{YL})}{4(2 + \cos\theta_{YL})} R_{III}$$

$$= \frac{4}{3}C_g \pi \rho g R_0^4 + 4C_s \pi \gamma R_0^2 + \frac{2}{3}C_k \pi \rho R_0^3 U_j^2 + 36.8 C_v \pi \mu \sqrt{\frac{\gamma R_0^3}{\rho}}. \tag{27}$$

Then the final form of the present model is given by

$$\frac{U_j}{U_c} = 0.898\eta^{-0.783}\left(\frac{3m}{2} - \frac{n}{2}\text{Bo} - 2.149\text{Oh}^{0.344}\eta^{2.212}\right)^{0.640}, \tag{28}$$

where

$$m = (2 - 2\cos\theta_{YL} - \sin^2\theta_{YL}\cos\theta_Y)k^2 - 4C_s, \tag{29}$$

$$n = C_g - \frac{(3 + \cos\theta_{YL})(1 - \cos\theta_{YL})k}{4(2 + \cos\theta_{YL})}. \tag{30}$$

It can be seen that U_j/U_c is determined by the joint effects of liquid properties, applied voltage, and substrate wettability, i.e., $U_j/U_c = f(\text{Bo}, \text{Oh}, \eta, \theta_Y)$. To validate the reliability of the present model, the comparison of the value of U_j/U_c predicted by Eq. (28) with numerical results is shown in Fig. 12(a). Notably, the present model shows good predicting performance, though the jumping velocity of water droplet with moderate R_0 is a little overestimated with an average relative error $\sim 12\%$. We believe that this error mainly results from the fitting of correction coefficient C_k, which is a little underestimated. In contrast, the prediction of Zhang's model [38], $U_j/U_c = [1.5A(\theta_Y, \theta_{YL}) - 6(1 + 4\text{Oh})]^{1/2}$, significantly overestimates the jumping velocity in the case of large R_0 due to the ignorance of gravity and shows pronounced underestimation in the case of small R_0 due to the inaccurate expression of viscous dissipation. Meanwhile, the neglected influence of droplet morphology on surface energy and gravitational potential energy also results in the overestimated U_j/U_c. In the above, $A(\theta_Y, \theta_{YL}) = k^2(2 - 2\cos\theta_{YL} - \sin^2\theta_{YL}\cos\theta_Y)$.

It is also observed from Fig. 12(a) that as R_0 becomes large, U_j/U_c first increases, then decreases, and its peak value arrives at moderate R_0. This observation demonstrates that the droplet with
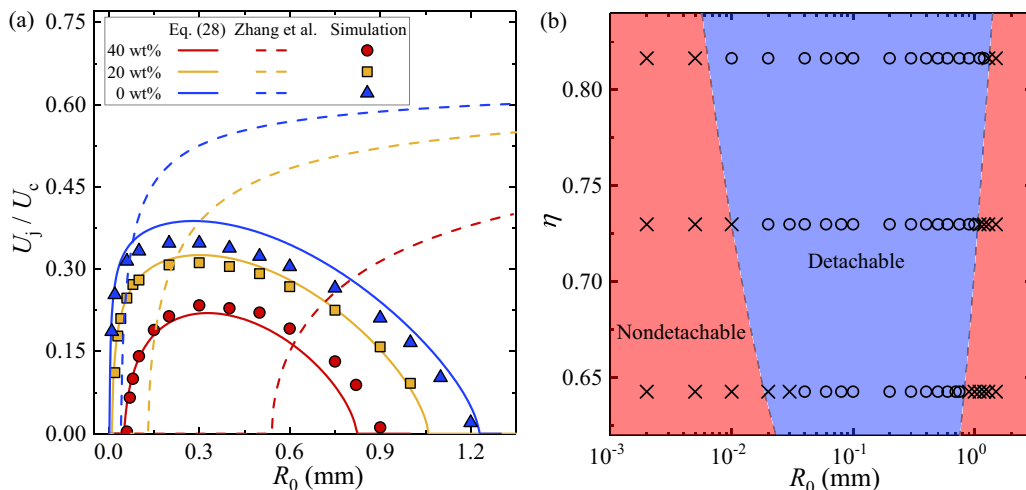
FIG. 12. (a) Comparison of the normalized jumping velocity estimated by Eq. (28) (solid lines) and Zhang's model [38] (dashed lines) with the simulated ones (solid symbol) under $\theta_{YL} = 85°$. (b) Phase diagram of detachable (circle) and nondetachable (cross) regimes in the parameter space spanned by R_0 and η. The dashed lines represent the critical conditions predicted by present model.

moderate size is easier to jump off the substrate and there are two critical conditions where the droplet begins to be nondetachable. We analyze that the existence of the smaller critical R_0 is due to the enhanced viscous dissipation, corresponding to high Oh, while the existence of the larger one is because of the prominent influence of gravity, corresponding to high Bo. On the contrary, the model of Zhang et al. [38] and other relevant models in the literature [17,37,39] fails to describe the nonmonotonic correlation of U_j/U_c with R_0 and the critical R_0 estimated by these models is unique, since they neglected the variation of gravitational potential energy or viscous dissipation.

The analysis above is on the basis of $\eta = 0.730$; whether the present model can still show good performance under various η deserves discussion. By substituting $U_j = 0$ into Eq. (28), the critical condition of droplet detachment can be solved. Figure 12(b) exhibits the phase diagram of detachable and nondetachable regimes in the parameter space spanned by R_0 and η, where the symbols denote the numerical results while the dashed lines denote the predictions of the present model. It is noteworthy that the critical conditions are well predicted under different η. Moreover, with the decrease of η, the larger critical R_0 decreases while the smaller critical R_0 increases, inducing a narrower detachable regime. We speculate that if the applied voltage continues to be reduced, the droplet may no longer be able to jump. A similar phenomenon has been reported by Wang et al. [18] and Vo et al. [37].

In this study, the intrinsic wettability of a solid surface is fixed with $\theta_Y = 130°$. Whether the present model is universal under various θ_Y and the advantages over previous models need to be further discussed. The electrowetting-induced detachment of a water droplet surrounded by silicone oil with a viscosity of 0.65 cSt was experimentally and numerically studied by Cavalli et al. [33]. According to their study, $V_{drop} = 5.5$ μL, $\rho = 1000$ kg/m³, $\gamma = 24.0$ mN/m, $\mu = 1.0$ mPa s, and $\theta_{YL} = 50°$ are used to predict U_j/U_c. Figure 13(a) shows the normalized jumping velocity as a function of substrate wettability, where the predictions of Eq. (28) and Zhang's model [38] are both displayed. Notably, the jumping velocity of Cavalli et al. [33] is significantly overestimated by Zhang et al. [38] and the overestimation can be attributed to the ignorance of the variation of gravitational potential energy and the uncorrected viscous dissipation. In contrast, the prediction of the present model is in good accordance with the previous work of Cavalli et al. [33], although the
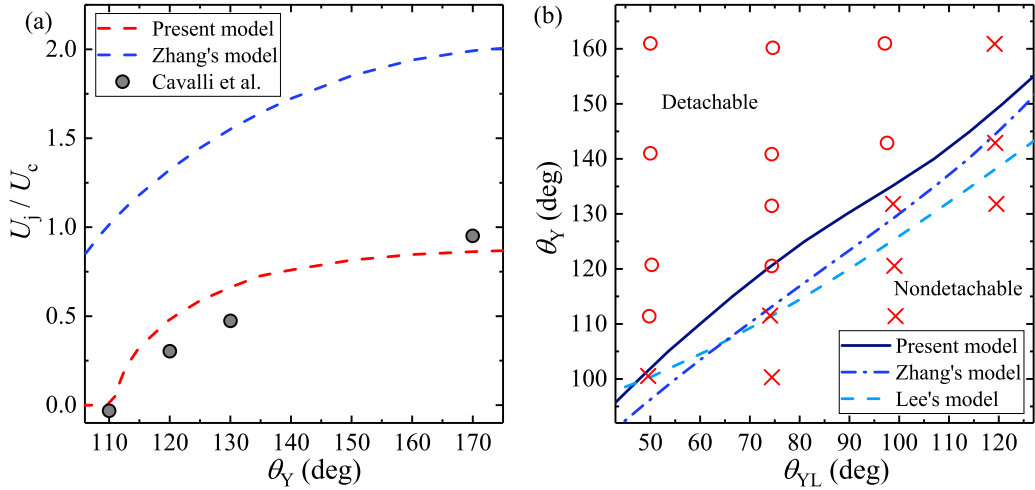
FIG. 13. (a) Comparison of the normalized jumping velocity estimated by Eq. (28) and Zhang's model [38] (dashed lines) with the previous work of Cavalli *et al.* [33] (solid symbol). (b) Phase diagram of detachable (circle) and nondetachable (cross) regimes in the parameter space spanned by θ_Y and θ_{YL}. The circle and cross symbols are obtained from the previous work of Nayak *et al.* [59]. The solid, dashed, and dashed-dotted lines represent the critical conditions predicted by present model, Zhang's model [38], and Lee's model [13], respectively. The volume of water droplet is 5.0 μL.

jumping velocity at $\theta_Y = 120°$ and $130°$ is slightly overestimated. We speculate that the predicting error can be explained by the influence of the surrounding silicone oil.

Furthermore, the critical conditions of a 5.0-μL water droplet under various θ_Y and θ_{YL} predicted by the present model, Zhang's model [38], and Lee's model [13] $\eta = 1 + \cos\theta_Y$ are shown in Fig. 13(b), which are compared with the numerical results of Nayak *et al.* [59]. Under the prediction of Lee's model [13], the droplet is the easiest to jump, since it completely neglects the viscous dissipation of entire recoiling and the variation of gravitational potential energy. The present model predicts the critical conditions of Nayak *et al.* [59] most accurately, whereas the critical θ_Y is underestimated by Zhang's model [38] due to neglecting the effect of gravity.

To examine the applicability of the present model for other fluids that are not used to fit the formulas of a correction coefficient, we simulate the electrowetting-induced detachment of silicone oil ($\rho = 760$ kg/m^3, $\gamma = 24$ mN/m, $\mu = 0.49$ mPa s [33]) and Galinstan ($\rho = 6440$ kg/m^3, $\gamma = 718$ mN/m, $\mu = 2.4$ mPa s [60]) droplets. In such cases, $\theta_Y = 130°$ and $\theta_Y = 85°$. As shown in Fig. 14, the values of normalized jumping velocity predicted by Eq. (28) are also in good agreement with the ones measured in the simulation. Accordingly, it is confirmed that the present model has good universality and the applicability can be extended to a variety of fluids.

Hence, the analysis and validation above demonstrate that after systematic corrections, the renewed model has shown good performance to predict the jumping velocity and critical condition of electrowetting-induced detachment under various conditions including liquid properties, applied voltage, droplet volume, and surface wettability. However, a subsequent improvement is also needed when applying the present model to the cases with high contact angle hysteresis and high-viscosity oil bath, since the present model does not take into account the energy loss due to contact line pinning and the viscous dissipation of the surrounding fluid.

Finally, to identify whether there will be any substantive difference in the prediction results, when the correction of different energy components is entirely neglected, we display Figs. 15(a)–15(d), which compare the simulated jumping velocity with the ones predicted by Eq. (27) under $C_g = 1$, $C_s = 1$, $C_v = 1$, $C_k = 1$, respectively. Meanwhile, the average value of relative error for each case is shown in Fig. 15(e). Here, the relative error is evaluated by dividing the difference between the
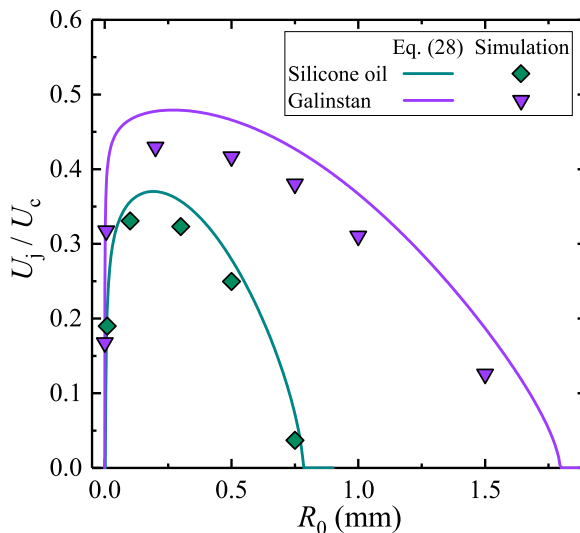
FIG. 14. Comparison of the normalized jumping velocity estimated by Eq. (28) (solid lines) with the simulated ones (solid symbol) under $\theta_{YL} = 85°$ for silicone oil and Galinstan.

simulated U_j/U_c and the predicted U_j/U_c by the simulated U_j/U_c. Noted from Fig. 15(a), when $C_g = 1$, the prediction of Eq. (27) is generally overestimated especially under large R_0, where gravity plays a more important role. On the contrary, when the surface energy term is not corrected, prominent errors appear mainly under relatively small droplets, since surface tension is more dominant in such a case [see Fig. 15(b)]. It is noteworthy from Fig. 15(c) that if the correction of viscous dissipation term is ignored, the prediction results will undergo a substantial change, since the numerous detachable droplets in the simulation become nondetachable in the estimation. Besides, as shown in Fig. 15(d), neglecting the correction of the kinetic energy term has a slight influence on the critical conditions of a jumping droplet, whereas it will cause a generally overestimated jumping velocity.

It is seen from Fig. 15(e) that without correction, each energy term will induce a considerable prediction error. Particularly, correcting viscous dissipation has a great influence on the prediction results, which reduces the relative error from ~10% to ~100%. In contrast, the relative errors introduced from the surface energy, gravitational potential energy, and kinetic energy at detachment are comparable, approaching 20%. Additionally, the sensitive analysis and statistical results shown in Figs. 15(b) and 15(e) verify the elaboration forementioned in Sec. IV B, i.e., although the relative deviation between the surface energy at detachment quantified by Eq. (3) and the one measured in the simulation is only ~0.5%, it is still necessary to correct the surface energy term.

V. CONCLUSIONS

In this study, we theoretically and numerically investigate the jumping velocity of an electrowetting-actuated droplet. The numerical simulation is conducted for three glycerol-water mixtures with initial radius $R_0 = 10\ \mu$m–1.40 mm actuated by three applied voltages on a hydrophobic surface. The examined Ohnesorge number Oh, Bond number Bo, and electrowetting number η range 0.003–0.07, 0.001–1.05, and 0.643–0.816, respectively. Based on the energy balance approach, we derive an analytical model that unifies the influence of liquid properties, droplet size, and applied voltage to predict the jumping velocity, which has been validated with both present simulation and the experiment in the literature. The present model demonstrates that the normalized jumping velocity U_j/U_c has a nonmonotonic relationship with droplet size, which first
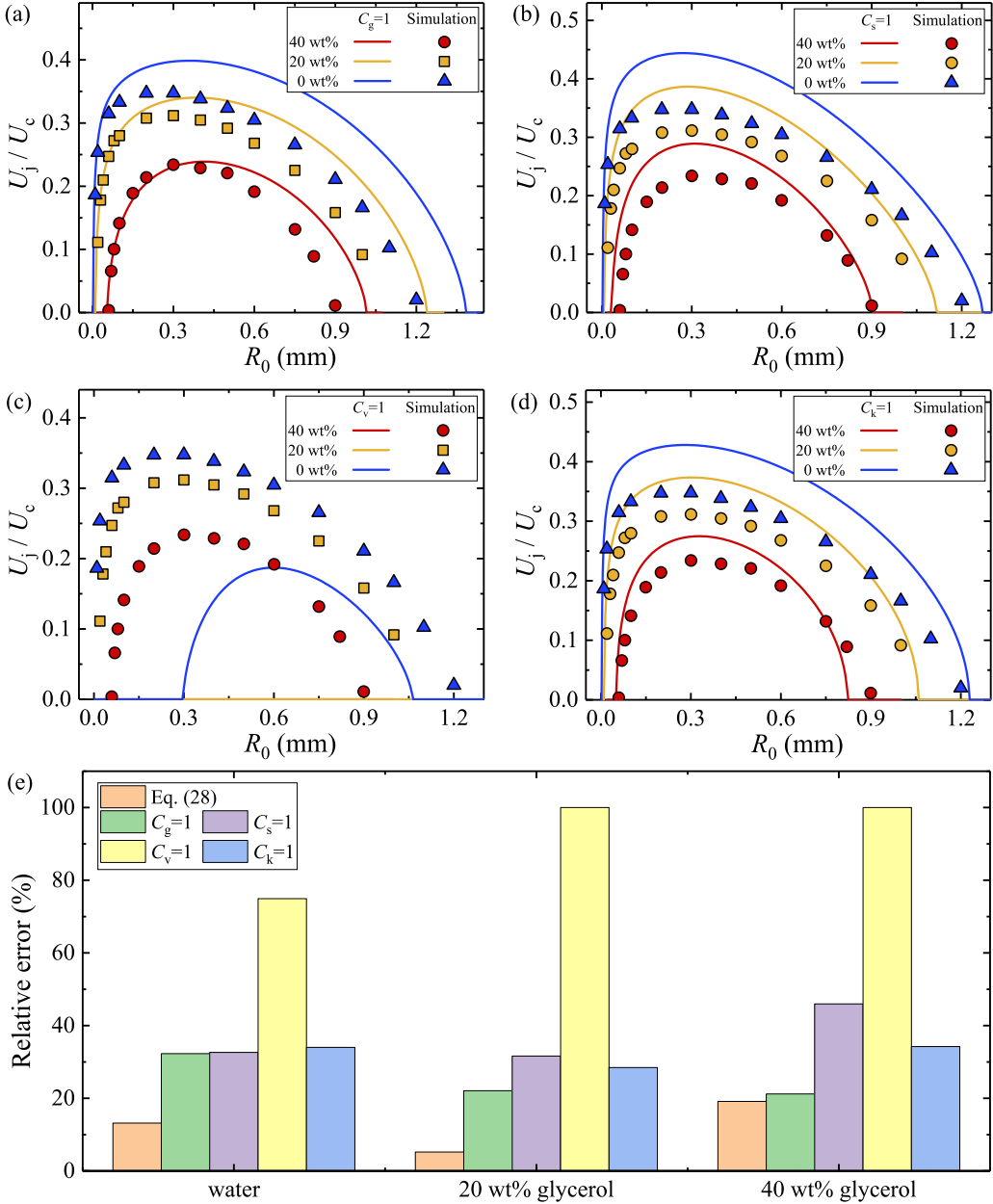
FIG. 15. Comparison of the value of U_j/U_c estimated by Eq. (27) (solid lines) when (a) $C_g = 1$, (b) $C_s = 1$, (c) $C_v = 1$, and (d) $C_k = 1$ with the simulated ones (solid symbol) under $\theta_{YL} = 85°$. (e) The average value of relative error of present model when neglecting the correction of different energy components.

increases due to the weakened viscous dissipation, then decreases due to the prominent influence of gravity. Hence, medium-sized droplets leave the substrate much more easily. In addition, the jumping velocity is enhanced by reducing the liquid viscosity and applying higher voltage. However, due to the saturation effect of contact angle, the jumping velocity will not increase continuously with the increase of the applied voltage [18].

Our main contribution is to reformulate the models of surface energy, gravitational potential energy, and kinetic energy at detachment, as well as the viscous dissipation of entire recoiling by introducing four correction coefficients. Although the formulas of correction coefficients are empirical, it is noteworthy that the applicability of present model can be extended to predict the jumping velocity of silicone oil and Galinstan droplets, which is not used for fitting. More importantly, we physically clarify the necessities to correct them. On the one hand, the simplification of spherical shape for jumping droplet leads to the underestimation of surface energy and gravity potential energy, since the droplet at detachment actually resembles a balloon. The correction coefficients of these two components are determined by Bond number Bo and electrowetting number η, which first increase, then decrease with the increase of Bo. On the other hand, we demonstrate that the assumption of constant velocity gradient during recoiling can account for the overestimated viscous dissipation by the previous model of Zhang *et al.* [38]. By substituting the recoiling time $t_d = (2.37 \pm 0.20)\,\tau_c$ and the associated correction coefficient scaled by $\text{Oh}^{-0.656}\eta^{2.212}$ into previous model, the formulation of viscous dissipation is refined. Furthermore, the kinetic energy at detachment is generally underestimated by the rigid body model since the contribution of radial velocity is neglected. Through the regression analysis, we find that the correction coefficient of kinetic energy follows the power law of electrowetting number and normalized jumping velocity. According to the error analysis, correcting the viscous dissipation term reduces the prediction error by $\sim$90%, while the relative error introduced from the other three energy terms are comparable, approaching $\sim$20%.

The numerical result indicates that at initial recoiling, the surface energy is rapidly converted into kinetic energy and gravitational potential energy, where the retraction dynamics is dominated by the balance of inertial force and capillary force. Consequently, the temporal evolution of contact radius is scaled by $R_c/R_{c,\text{III}} = 1 - 0.425\,(t/\tau_c)^{0.592}$. The propagation of capillary wave along the droplet interface is also observed during initial recoiling, which is less visible for smaller droplet due to stronger viscous damping. At late recoiling, the kinetic energy is reduced to overcome adhesion work and gravity. Throughout the recoiling and the process after detachment, viscous dissipation continues to increase. In our future work, we will focus on how to improve the energy conversion efficiency of electrowetting-induced detachment and how to reduce energy consumption as much as possible under the premise of similar jumping velocity.

[1] D. Baratian, R. Dey, H. Hoek, D. van den Ende, and F. Mugele, Breath Figures under Electrowetting: Electrically Controlled Evolution of Drop Condensation Patterns, Phys. Rev. Lett. **120**, 214502 (2018).

[2] N. Miljkovic, D. J. Preston, R. Enright, and E. N. Wang, Electric-field-enhanced condensation on superhydrophobic nanostructured surfaces, ACS Nano **7**, 11043 (2013).

[3] R. Dey, J. Gilbers, D. Baratian, H. Hoek, and D. van den Ende, Controlling shedding characteristics of condensate drops using electrowetting, Appl. Phys. Lett. **113**, 243703 (2018).

[4] J. B. Boreyko and C. H. Chen, Self-Propelled Dropwise Condensate on Superhydrophobic Surfaces, Phys. Rev. Lett. **103**, 184501 (2009).

[5] K. M. Wisdom, J. A. Watson, X. Qu, F. Liu, G. S. Watson, and C. H. Chen, Self-cleaning of superhydrophobic surfaces by self-propelled jumping condensate, Proc. Natl. Acad. Sci. USA **110**, 7992 (2013).

[6] I. Frozanpoor, M. D. Cooke, V. Ambukan, A. J. Gallant, and C. Balocco, Continuous droplet-actuating platforms via an electric field gradient: Electrowetting and liquid dielectrophoresis, Langmuir **37**, 6414 (2021).

[7] A. Lafuma and D. Quer´e, Slippery pre-suffused surfaces, Europhys. Lett. **96**, 56001 (2011).

[8] J. Hong, Y. K. Kim, D. J. Won, J. Kim, and S. J. Lee, Three-dimensional digital microfluidic manipulation of droplets in oil medium, Sci. Rep. **5**, 10685 (2015).

[9] K. Wang and J. Li, Electricity generation from the interaction of liquid–solid interface: A review, J. Mater. Chem. A **9**, 8870 (2021).

[10] J. Hong and S. J. Lee, Detaching droplets in immiscible fluids from a solid substrate with the help of electrowetting, Lab Chip **15**, 900 (2015).

[11] A. J. James, B. Vukasinovic, M. K. Smith, and A. Glezer, Vibration-induced drop atomization and bursting, J. Fluid Mech. **476**, 1 (2003).

[12] A. Glière, J. M. Roux, and J. L. Achard, Lift-off of a conducting sessile drop in an electric field, Microfluid. Nanofluid. **15**, 207 (2013).

[13] S. J. Lee, S. Lee, and K. H. Kang, Jumping of a droplet on a superhydrophobic surface in AC electrowetting, J. Vis. **14**, 259 (2011).

[14] P. Teng, D. Tian, H. Fu, and S. Wang, Recent progress of electrowetting for droplet manipulation: From wetting to superwetting systems, Mat. Chem. Front. **4**, 140 (2020).

[15] J. Li, Current commercialization status of electrowetting-on-dielectric (EWOD) digital microfluidics, Lab Chip **20**, 1705 (2020).

[16] Z. Wang, D. van den Ende, A. Pit, R. Lagraauw, D. Wijnperléa, and Frieder Mugele, Jumping drops on hydrophobic surfaces, controlling energy transfer by timed electric actuation, Soft Matter **13**, 4856 (2017).

[17] S. J. Lee, J. Hong, K. H. Kang, I. S. Kang, and S. J. Lee, Electrowetting-induced droplet detachment from hydrophobic surfaces, Langmuir **30**, 1805 (2014).

[18] Q. Wang, M. Xu, C. Wang, J. Gu, N. Hu, J. Lyu, and W. Yao, Actuation of a nonconductive droplet in an aqueous fluid by reversed electrowetting effect, Langmuir **36**, 8152 (2020).

[19] L. Chen and E. Bonaccurso, Electrowetting—From statics to dynamics, Adv. Colloid Interface Sci. **210**, 2 (2014).

[20] M. G. Lippmann, Relation entre les phénomènes électriques et capillaires, Ann. Chim. Phys. **5**, 494 (1875).

[21] A. Frumkin, A. Gorodetskaya, B. Kabanov, and N. Nekrasov, Electrocapillary phenomena and the wetting of metals by electrolytic solutions, I, Phys. Z. Sowjetunion **1**, 255 (1932).

[22] N. Laan, K. G. de Bruin, D. Bartolo, C. Josserand, and D. Bonn, Maximum Diameter of Impacting Liquid Droplets, Phys. Rev. Appl. **2**, 044018 (2014).

[23] M. Pasandideh-Fard, Y. M. Qiao, S. Chandra, and J. Mostaghimi, Capillary effects during droplet impact on a solid surface, Phys. Fluids **8**, 650 (1996).

[24] C. Ukiwe and D. Y. Kwok, On the maximum spreading diameter of impacting droplets on well-prepared solid surfaces, Langmuir **21**, 666 (2005).

[25] F. Wang, L. Yang, L. Wang, Y. Zhu, and T. Fang, Maximum spread of droplet impacting onto solid surfaces with different wettabilities: Adopting a rim–lamella shape, Langmuir **35**, 3204 (2019).

[26] S. Wildeman, C. W. Visser, C. Sun, and D. Lohse, On the spreading of impacting drops, J. Fluid Mech. **805**, 636 (2016).

[27] I. V. Roisman, R. Rioboo, and C. Tropea, Normal impact of a liquid drop on a dry surface: Model for spreading and receding, Proc. R. Soc. London Ser. A **458**, 1411 (2002).

[28] D. Richard and D. Quéré, Bouncing water drops, Europhys. Lett. **50**, 769 (2000).

[29] C. Hao, J. Li, Y. Liu, X. Zhou, Y. Liu, R. Liu, L. Che, W. Zhou, D. Sun, L. Li, and Z. Wang, Superhydrophobic-like tunable droplet bouncing on slippery liquid interfaces, Nat. Commun. **6**, 7986 (2015).

[30] T. M. Schutzius, S. Jung, T. Maitra, G. Graeber, M. Kohme, and D. Poulikakos, Spontaneous droplet trampolining on rigid superhydrophobic surfaces, Nature (London) **527**, 82 (2015).

[31] J. de Ruiter, R. Lagraauw, D. van den Ende, and F. Mugele, Wettability-independent bouncing on flat surfaces mediated by thin air films, Nat. Phys. **11**, 48 (2015).

[32] J. de Ruiter, R. Lagraauw, F. Mugele, and D. van den Ende, Bouncing on thin air: How squeeze forces in the air film during non-wetting droplet bouncing lead to momentum transfer and dissipation, J. Fluid Mech. **776**, 531 (2015).

[33] A. Cavalli, D. J. Preston, E. Tio, D. W. Martin, N. Miljkovic, E. N. Wang, F. Blanchette, and J. W. M. Bush, Electrically induced drop detachment and ejection, Phys. Fluids **28**, 022101 (2016).

[34] N. Weng, Q. Wang, J. Gu, J. Li, C. Wang, and W. Yao, The dynamics of droplet detachment in reversed electrowetting (REW), Colloid Surf. A **616**, 126303 (2021).

[35] A. Merdasi, M. A. Daeian, A. Moosavi, and M. B. Shafii, Electrowetting induced droplet jumping over a bump, Extreme Mech. Lett. **32**, 100538 (2019).

[36] A. Merdasi, A. Moosavi, and M. B. Shafii, Electrowetting-induced droplet jumping over topographically structured surfaces, Mater. Res. Express **6**, 086333 (2019).

[37] Q. Vo and T. Tran, Critical Conditions for Jumping Droplets, Phys. Rev. Lett. **123**, 024502 (2019).

[38] K. Zhang, Z. Li, and S. Chen, Analytical prediction of electrowetting-induced jumping motion for droplets on hydrophobic substrates, Phys. Fluids **31**, 081703 (2019).

[39] C. T. Burkhart, K. L. Maki, and M. J. Schertzer, Coplanar electrowetting-induced droplet detachment from radially symmetric electrodes, Langmuir **36**, 8129 (2020).

[40] N. T. Chamakos, M. E. Kavousanakis, A. G. Boudouvis, and A. G. Papathanasiou, Droplet spreading on rough surfaces: Tackling the contact line boundary condition, Phys. Fluids **28**, 022105 (2016).

[41] G. Karapetsas, N. T. Chamakos, and A. G. Papathanasiou, Efficient modelling of droplet dynamics on complex surfaces, J. Phys.: Condens. Matter **28**, 085101 (2016).

[42] A. G. Sourais and A. G. Papathanasiou, Modelling of electrowetting-induced droplet detachment and jumping over topographically micro-structured surfaces, Micromachines **12**, 592 (2021).

[43] N. T. Chamakos, D. G. Sema, and A. G. Papathanasiou, Progress in modeling wetting phenomena on structured substrates, Arch. Comput. Method Eng. **28**, 1647 (2021).

[44] J. Du, Y. Zhang, and Q. Min, Numerical investigations of the spreading and retraction dynamics of viscous droplets impact on solid surfaces, Colloid Surf. A **609**, 125649 (2021).

[45] J. Du, N. T. Chamakos, A. G. Papathanasiou, and Q. Min, Initial spreading dynamics of a liquid droplet: The effects of wettability, liquid properties, and substrate topography, Phys. Fluids **33**, 042118 (2021).

[46] J. Du, X. Wang, Y. Li, and Q. Min, Maximum spreading of liquid droplets impact on concentric ring-textured surfaces: Theoretical analysis and numerical simulation, Colloid Surf. A **630**, 127647 (2021).

[47] J. Du, X. Wang, Y. Li, and Q. Min, Analytical consideration for the maximum spreading factor of liquid droplet impact on a smooth solid surface, Langmuir **37**, 7582 (2021).

[48] A. Riaud, C. Wang, J. Zhou, W. Xu, and Z. Wang, Hydrodynamic constraints on the energy efficiency of droplet electricity generators, Microsyst. Nanoeng. **7**, 49 (2021).

[49] V. M. Starov, Surface forces action in a vicinity of three phase contact line and other current problems in kinetics of wetting and spreading, Adv. Colloid Interface Sci. **161**, 139 (2010).

[50] T. J. O'Sullivan, S. K. Kannam, D. Chakraborty, and B. D. Todd, Viscoelasticity of liquid water investigated using molecular dynamics simulations, Phys. Rev. Fluids **4**, 123302 (2019).

[51] E. Fares and W. Schroder, A differential equation for approximate wall distance, Int. J. Numer. Methods Fluids **39**, 743 (2002).

[52] L. Chen and E. Bonaccurso, Effects of surface wettability and liquid viscosity on the dynamic wetting of individual drops, Phys. Rev. E **90**, 022401 (2014).

[53] J. C. Bird, S. Mandre, and H. A. Stone, Short-Time Dynamics of Partial-Wetting, Phys. Rev. Lett. **100**, 234501 (2008).

[54] D. Wheeler, J. A. Warren, and W. J. Boettinger, Modeling the early stages of reactive wetting, Phys. Rev. E **82**, 051601 (2010).

[55] S. J. Lee, S. Lee, and K. H. Kang, Droplet jumping by electrowetting and its application to the three-dimensional digital microfluidics, Appl. Phys. Lett. **100**, 081604 (2012).

[56] A. K. Raman, R. K. Jaiman, T. S. Lee, and H. T. Low, A numerical study on electrowetting-induced jumping and transport of droplet, Int. J. Heat Mass Transfer **99**, 805 (2016).

[57] M. A. Islam and A. Y. Tong, A numerical study on electrowetting-induced droplet detachment from hydrophobic surface, J. Heat Transfer Trans. ASME **140**, 052003 (2018).

[58] D. Legendre and M. Maglio, Numerical simulation of spreading drops, Colloids Surf., A **432**, 29 (2013).

[59] S. G. Nayak and J. Banerjee, Numerical analysis of droplet detachment from hydrophobic surfaces during electrowetting, Multiphase Sci. Technol. **33**, 19 (2021).

[60] L. Zhu, B. Wang, S. Handschuh-Wang, and X. Zhou, Liquid metal–based soft microfluidics, Small **16**, 1903841 (2020).